

Plasma Diagnostics of the Supernova Remnant N132D Using Deep XMM–Newton Observations with the Reflection Grating Spectrometer

HITOMI SUZUKI,^{1,2} HIROYA YAMAGUCHI,^{2,3} MANABU ISHIDA,^{1,2} HIROYUKI UCHIDA,⁴ PAUL P. PLUCINSKY,⁵
ADAM R. FOSTER,⁵ AND ERIC D. MILLER⁶

¹*Department of Physics, Tokyo Metropolitan University, 1-1 Minami-Osawa, Hachioji, Tokyo 192-0397, Japan*

²*The Institute of Space and Astronautical Science (ISAS), Japan Aerospace and Exploration Agency (JAXA), 3-1-1 Yoshinodai, Chuo-ku, Sagami-hara 299-8510, Japan*

³*Department of Physics, The University of Tokyo, 7-3-1 Hongo, Bunkyo-ku, Tokyo 113-0033, Japan*

⁴*Department of Physics, Kyoto University, Kitashirakawa Oiwake-cho, Sakyo-ku, Kyoto 606-8502, Japan*

⁵*Center for Astrophysics — Harvard & Smithsonian, 60 Garden St., Cambridge, MA 02138, USA*

⁶*Kavli Institute for Astrophysics and Space Research, Massachusetts Institute of Technology, 77 Massachusetts Ave., Cambridge, MA 02139, USA*

(Received; Revised; Accepted)

Submitted to ApJ

ABSTRACT

We present XMM–Newton observations of N132D, the X-ray brightest supernova remnant (SNR) in the Large Magellanic Cloud (LMC), using the Reflection Grating Spectrometer (RGS) that enables high-resolution spectroscopy in the soft X-ray band. A dozen emission lines from L-shell transitions of various elements at intermediate charge states are newly detected in the RGS data integrating the ~ 200 -ks on-axis observations. The 0.3–2.0-keV spectra require at least three components of thermal plasmas with different electron temperatures and indicate clear evidence of non-equilibrium ionization (NEI). Our detailed spectral diagnostics further reveal that the forbidden-to-resonance line ratios of O VII and Ne IX are both higher than expected for typical NEI plasmas. This enhancement could be attributed to either resonance scattering or emission induced by charge exchange in addition to a possible contribution from the superposition of multiple temperature components, although the lack of spatial information prevents us from concluding which is most likely.

Keywords: ISM: individual objects (N132D) — ISM: supernova remnants — X-rays: ISM

1. INTRODUCTION

High-resolution spectroscopy of supernova remnants (SNRs) using X-ray grating spectrometers has enabled detailed plasma diagnostics, providing insights into the shock physics and radiation processes in the hot plasmas that consist of the supernova ejecta and ambient medium (e.g., Vink et al. 2003; Katsuda et al. 2012; Miceli et al. 2019; Uchida et al. 2019). In particular, the Reflection Grating Spectrometer (RGS) on board the XMM–Newton satellite is suitable for observing moderately extended objects (a few arcmin in diameter), like SNRs in the Large Magellanic Cloud (LMC) because of its relatively large dispersion angle (den Herder et al. 2001; Rasmussen et al. 2001). N132D, a middle-aged SNR located in the stellar bar of the LMC, is one of such objects, owing to its high luminosity in the X-ray band as well as the moderate angular diameter of $\sim 2'$. In this paper, we present high-resolution spectroscopy of this SNR, utilizing the excellent features of the RGS.

Optical studies of N132D estimated its age to be 2500–3100 yrs based on the expansion of the O-rich knots (Morse et al. 1995; Vogt & Dopita 2011; Law et al. 2020). Hubble Space Telescope observations revealed the strong emission of the C/Ne-burning products (i.e., O, Ne, Mg) with little emission of the O-burning products (i.e., Si, S), lead-

ing to an interpretation of a Type Ib supernova origin for this SNR (Blair et al. 2000). The X-ray emission from N132D was first identified by the Einstein Observatory, which also revealed the clear shell-like morphology (Mathewson et al. 1983). Using ASCA, Hughes et al. (1998) found that the elemental abundances of the entire SNR are consistent with the mean LMC values (Russell & Dopita 1992), suggesting that the emission in the soft X-ray band ($\lesssim 2$ keV) is dominated by the swept-up interstellar medium (ISM). On the other hand, the Fe K emission, first detected by BeppoSAX (Favata et al. 1997), shows a more centrally concentrated morphology (Behar et al. 2001; Borkowski et al. 2007; Sharda et al. 2020), suggesting an ejecta origin of this emission. The Suzaku and NuSTAR studies of this SNR detected Ly α emission from H-like Fe, alongside the stronger He-like K-shell emission (Bamba et al. 2018). Notably, the K-shell emission from highly-ionized Fe is a common feature of core-collapse SNRs (Yamaguchi et al. 2014), consistent with the optical studies of this SNR (e.g., Vogt & Dopita 2011). More recently, Hitomi observations utilizing the remarkably high spectral resolution of the micro-calorimeter (but with an extremely short exposure) revealed that the Fe K emission is substantially redshifted with respect to the local LMC ISM (Hitomi Collaboration et al. 2018a), implying an asymmetric explosion of the progenitor of this SNR.

Similarly to other core-collapse SNRs, N132D is located within a dense environment. Infrared and radio studies revealed that the south rim of this SNR is interacting with particularly dense clouds (Williams et al. 2006; Sano et al. 2015), whose pre-shock density is estimated to be $100\text{--}500\text{ cm}^{-3}$, depending on the direction (Dopita et al. 2018). X-ray studies also indicated that the SNR has expanded into a cavity formed by the pre-explosion stellar wind activity of the progenitor and reached the cavity wall recently (Hughes et al. 1998; Chen et al. 2003). The strong interaction between the SNR shock and dense clouds is also suggested by the bright GeV and TeV γ -ray emission possibly originating from hadronic processes (Ackermann et al. 2016; H. E. S. S. Collaboration et al. 2015); N132D is indeed the brightest in γ -ray among all known SNRs (Acero et al. 2016). We may, therefore, independently find a signature of such SNR-ISM interaction in its soft X-ray spectrum, which is one of our motivations for the present study.

The early RGS observations of N132D, conducted as a part of the Performance Verification program of XMM–Newton with the total effective exposure of ~ 50 ks, were reported by Behar et al. (2001). They identified the spectral lines of C, N, O, Ne, Mg, Si, S, and Fe in $6\text{--}37\text{ \AA}$ (corresponding to the photon energy of $0.34\text{--}2.0$ keV) and revealed the wide range of Fe charge states ($\text{Fe}^{16+}\text{--}\text{Fe}^{21+}$) that indicates the presence of multiple electron temperatures. In the previous work, however, first- and second-order spectra with different resolutions were summed in the analysis, and no quantitative spectral modeling was performed to determine whether the plasma was in collisional ionization equilibrium (CIE) or non-equilibrium ionization (NEI). Moreover, while N132D has been routinely observed by XMM–Newton for the instrumental calibration purpose, the scientific outcome from these observations (whose net exposure exceeds 1 Ms) has never been reported to date. Thus, here we analyze all the available RGS data with a more quantitative approach that simultaneously models first and second order. In particular, the high-resolution second-order spectrum enables detailed diagnostics using the well-separated emission lines, revealing clear evidence of NEI and a possible signature of additional effects that have modified the line intensity ratios between the forbidden and resonance emission, such as resonance scattering and/or charge exchange.

This paper is organized as follows. Sections 2 and 3 describe the data reduction and response generation, respectively. In Section 4, we perform spectral analysis based on realistic plasma models. We then conduct detailed spectral diagnostics using several strong lines and discuss the results in Section 5. Finally, we conclude this study in Section 6. Throughout the paper, we assume the distance to the LMC to be 50 kpc (Pietrzyński et al. 2013). The errors quoted in the text and table and error bars given in the figures represent the 1σ confidence level, unless otherwise stated.

2. DATA REDUCTION

The primary purposes of the routine observations of N132D with XMM–Newton are the gain, spectral redistribution, and effective area calibrations of the European Photon Imaging Camera (EPIC). Therefore, although the high-resolution spectral data with the RGS were simultaneously obtained, the SNR was placed outside or near the edge of the field of view of the RGS in most of these observations. Since our aim is to analyze the high-resolution grating spectra, we use only the datasets where the target was observed on the optical axis of the telescope.

The data are reprocessed using the `rgsproc` task in the XMM–Newton Science Analysis Software (XMM-SAS) version 18.0.0 and the Current Calibration Files (CCF). We extract background light curves using the standard procedure¹ and filter out observation periods when the background count rate is higher than 0.1 cnt s^{-1} . In addition, we discard

¹ https://xmm-tools.cosmos.esa.int/external/xmm_user_support/documentation/sas-usg/USG/rgslightcurve.html

Table 1. Observation log.

Observation ID	Date	Roll angle (deg)	Exposure* (ks)
0125100201	2000 May 23	339.77	13.63
0157160601	2002 Nov 16	152.29	26.20
0157160801	2002 Nov 24	160.35	29.09
0157161001	2002 Dec 14	180.55	29.91
0157360201	2002 Dec 31	196.82	15.02
0157360301	2003 Jan 17	215.16	28.66
0157360501	2003 Feb 22	251.66	14.92
0129341301	2003 Sep 13	88.84	20.34
0137551101	2004 Sep 8	88.76	15.04

NOTE—*Effective exposure after the screening (see text).

Observation IDs whose exposure time after the screening is less than 10 ks. The observations that meet these criteria are given in Table 1, obtaining the total effective exposure of 193 ks for both the RGS1 and RGS2.

We extract the first- and second-order RGS spectra of each observation from the region centered on $(RA, Dec)_{J2000} = (05\ 25\ 03.96, -69\ 38\ 29.6)$ with the cross-dispersion width of $2'2$ to contain the entire SNR regardless of the roll angle. Figure 1 shows the resulting spectra, where the data from all the observations (193 ks) are integrated to improve the photon statistics. The detected emission lines are summarized in Table 2, together with their centroid energy and identified atomic transition. In addition to the lines already reported by Behar et al. (2001), we have newly detected a dozen L-shell emission from Fe and the intermediate-mass elements as well as weak K-shell emission of high- n transitions. Notably, the Ne IX forbidden and resonance lines are clearly resolved for the first time, owing to the better energy resolution of the second-order spectrum ($\Delta E = 9.9\text{ eV}$ at 0.9 keV for an extended object with an angular diameter of $2'2$, which is about twice better than the first-order’s energy resolution). This allows us to put strong constraints on the important spectral parameters, such as electron temperature and ionization timescale, as demonstrated in the following sections.

3. RESPONSE GENERATION

This section describes how we treat the spectral response, which is crucial for the accurate spectral analysis presented in the following sections. In general, grating spectrometers are utilized for observing point-like sources, and thus a response matrix generated by the standard processes in the `rgsproc` task is not applicable to analysis of morphologically asymmetric, extended objects, like N132D. Therefore, we convolve the standard response matrix (valid for point-like sources) with the projected profiles of the surface brightness along the dispersion axis ((Figure 2), using the publicly-available script `ftgrsrmfsmooth`². This process is executed for each Obs.ID independently, since the projected profile depends on the roll angle. We find, furthermore, that the morphology of the SNR varies with energy range, as illustrated in (Figure 2. To account for this issue, we generate projected profiles using archived Chandra images (that have the highest available angular resolution) in the five energy ranges of 0.32–0.6 keV, 0.6–0.7 keV, 0.7–0.85 keV, 0.85–1.0 keV, and 1.0–2.0 keV. No significant difference is found in the projected profiles of even narrower energy bands. Accordingly, we generate convolved response matrices for each of the RGS1 and RGS2 and each of the first- and second-order spectra. In the subsequent spectral analysis, we apply these responses to the spectra in the corresponding energy bands.

4. SPECTRAL MODELING

Although we have made the best effort to generate the spectral response for this extended object, the roll angle dependence of the line spread function may still cause substantial uncertainties in the modeling. We therefore analyze

² <https://heasarc.gsfc.nasa.gov/lheasoft/ftools/fhelp/ftgrsrmfsmooth.html>

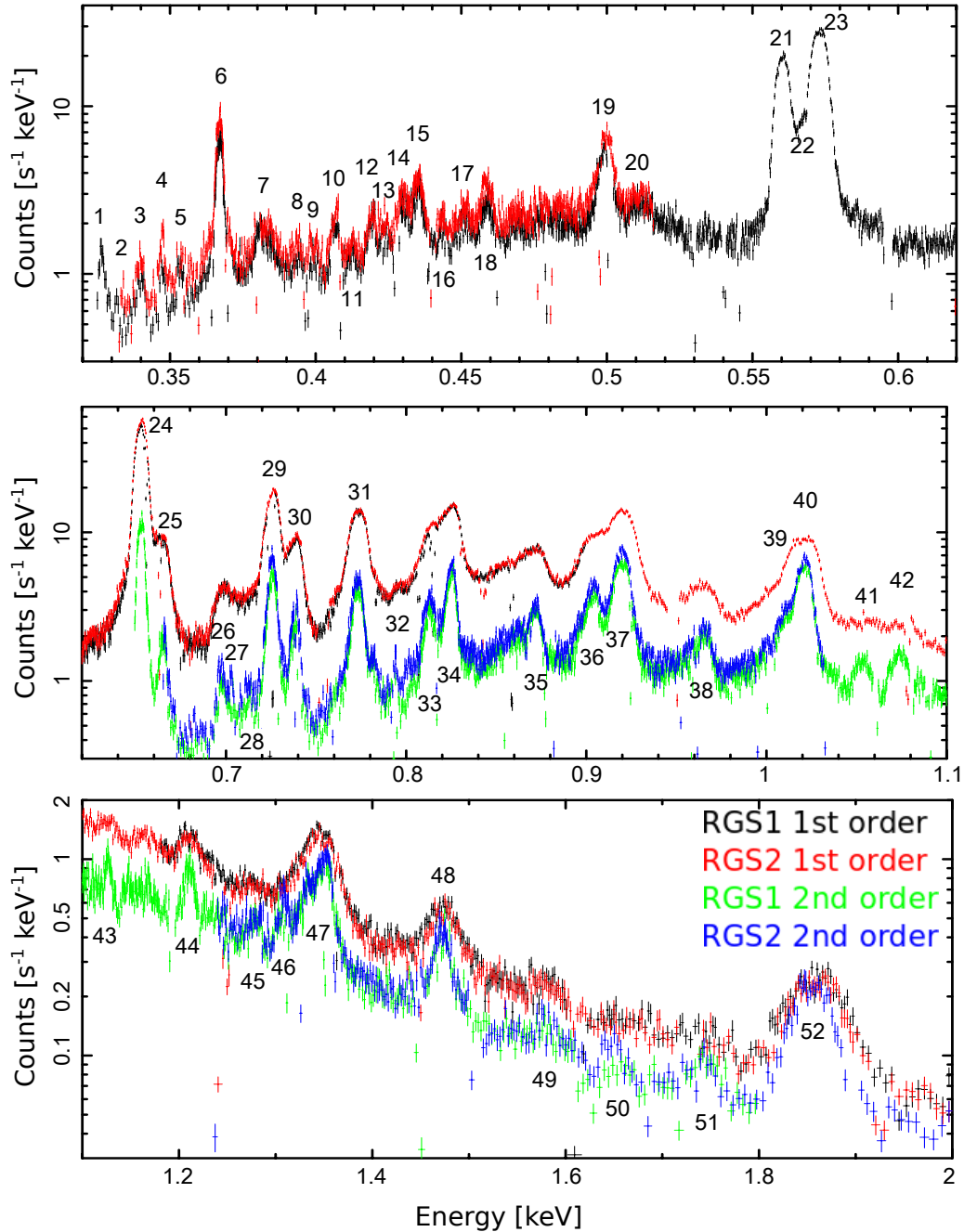


Figure 1. XMM-Newton RGS spectra where all the observations given in Table 1 are integrated. Black and red are the first-order spectra of the RGS1 and RGS2, respectively. Green and blue are the second-order spectra of these spectrometers, whose bandpass is limited to $\gtrsim 0.65$ keV. The detected lines are labeled and listed in Table 2 with their identification.

the spectra from each Obs. ID independently, rather than performing simultaneous spectral fitting, to investigate typical ranges of the systematic uncertainties (and later derive the mean values and deviations among the different Obs. IDs of the intensities of some strong lines). First, we analyze the data from the longest exposure (Obs. ID 0157161001) which had a roll angle of 180.55 deg. While the second-order spectra have better resolution, the first-order spectra cover a wider wavelength range particularly in the soft X-ray band. Therefore, we use the second-order spectra for their full bandpass (i.e., 0.66–2.0 keV) and the first-order spectra only when the second order is unavailable (i.e., 0.32–0.68 keV).

Table 2. Detected emission lines and their identification.

Label	Energy (keV)	Ion	Transition	Label	Energy (keV)	Ion	Transition	Label	Energy (keV)	Ion	Transition
1 *	0.329	S XIII	3s → 2p	20 *	0.511	S XIV	4d → 2p	37	0.917	Fe XIX	3d → 2p
2 *	0.332	Si XI	4d → 2p	21	0.561	O VII	2s → 1s (f)		0.922	Ne IX	2p → 1s (r)
3 *	0.341	S XII	3d → 2p	22	0.569	O VII	2p → 1s (i)	38	0.964	Fe XX	3d → 2p
4 *	0.347	Ca XI	3s → 2p	23	0.574	O VII	2p → 1s (r)		0.965	Fe XX	3d → 2p
5 *	0.352	Ca XI	3s → 2p	24	0.654	O VIII	2p → 1s	39 *	1.009	Fe XXI	3d → 2p
6	0.368	C VI	2p → 1s	25	0.666	O VII	3p → 1s	40	1.022	Ne X	2p → 1s
7	0.381	S XIV	3d → 2p	26 *	0.698	O VII	4p → 1s	41	1.053	Fe XXII	3d → 2p
8 *	0.395	Ar XII	3d → 2p	27	0.704	Fe XVIII	3p → 2p		1.056	Fe XXIII	3d → 2p
9 *	0.399	S XI	4d → 2p	28 *	0.713	O VII	5p → 1s	42	1.074	Ne IX	3p → 1s
10	0.407	S XIV	3p → 2s	29	0.725	Fe XVII	3s → 2p	43	1.127	Ne IX	4p → 1s
11 *	0.414	S XII	4s → 2p		0.727	Fe XVII	3s → 2p	44	1.211	Ne X	3p → 1s
12	0.420	N VI	2s → 1s (f)	30	0.739	Fe XVII	3s → 2p	45	1.277	Ne X	4p → 1s
13	0.426	N VI	2p → 1s (i)	31	0.775	Fe XVIII	3s → 2p	46 *	1.314	Fe XXI	4d → 2p
14	0.431	N VI	2p → 1s (r)		0.775	O VIII	3p → 1s	47	1.352	Mg XI	2p → 1s (r)
15	0.436	C VI	3p → 1s	32 *	0.793	Fe XVIII	3s → 2p	48	1.473	Mg XII	2p → 1s
16 *	0.443	Ca XII	3d → 2p	33	0.812	Fe XVII	3d → 2p	49 *	1.579	Mg XI	3p → 1s
17 *	0.451	Ar XIV	3d → 2p	34	0.826	Fe XVII	3d → 2p	50 *	1.659	Mg XI	4p → 1s
18	0.459	C VI	4p → 1s	35	0.873	Fe XVIII	3d → 2p	51 *	1.745	Mg XII	3p → 1s
19	0.500	N VII	2p → 1s	36	0.905	Ne IX	2s → 1s (f)	52	1.865	Si XIII	2p → 1s (r)

NOTE—The asterisk symbols indicate the emission lines that are newly detected in this work.

The XSPEC software version 12.10.0c and the C -statistic (Cash 1979) on unbinned spectra are used in the subsequent spectral analysis.

Since the previous RGS study indicated the presence of multiple-temperature plasmas (Behar et al. 2001), we start spectral modeling with two components of velocity-broadened, collisionally-ionized plasma models, `bvrnei`³ in the XSPEC package, that can reproduce both CIE and NEI plasmas. The free parameters are the electron temperature (kT_e), ionization parameter ($n_e t$) that is a product of the electron density and time elapsed after shock heating, abundances of C, N, O, Ne, Mg, Si, S, Ar, Ca, Fe and Ni relative to the solar values of Wilms et al. (2000), velocity dispersion σ , and the volume emission measure (VEM). The ionization parameters and abundances of each element of the two components are tied to each other. We also allow the redshift (or blueshift when the value is negative) of each plasma component to vary freely, although the resulting values could be dominated by the calibration uncertainties in the channel-to-wavelength transformation, rather than the real plasma motion. The initial plasma temperature (kT_{init}) is fixed to 0.01 keV (i.e., assuming that the plasma has been ionizing). For the foreground absorption, we introduce the `tbnew` models⁴ with solar (Wilms et al. 2000) and LMC (Russell & Dopita 1992; Schenck et al. 2016) abundances for the Galactic and LMC components, respectively. The hydrogen column density N_{H} of the former is fixed to $6.2 \times 10^{20} \text{ cm}^{-2}$ (Dickey & Lockman 1990), whereas that of the latter is left as a free parameter.

With these models and assumptions, we obtain the best-fit result with the electron temperatures of ~ 0.31 keV and ~ 0.91 keV, ionization parameter of $\sim 1.3 \times 10^{11} \text{ cm}^{-3} \text{ s}$, and C -stat/d.o.f. of 10962/7567. We find a significant discrepancy between the model and data particularly around 1.05 keV; the model (the black solid curve in Figure 3) fails to reproduce the emission lines of Fe^{21+} and Fe^{22+} at this energy. This indicates the presence of even hotter plasma where the Fe is more highly ionized. We thus add another NEI component with a different electron temperature, but

³ <https://heasarc.gsfc.nasa.gov/xanadu/xspec/manual/node145.html>

⁴ <https://pulsar.sternwarte.uni-erlangen.de/wilms/research/tbabs/>

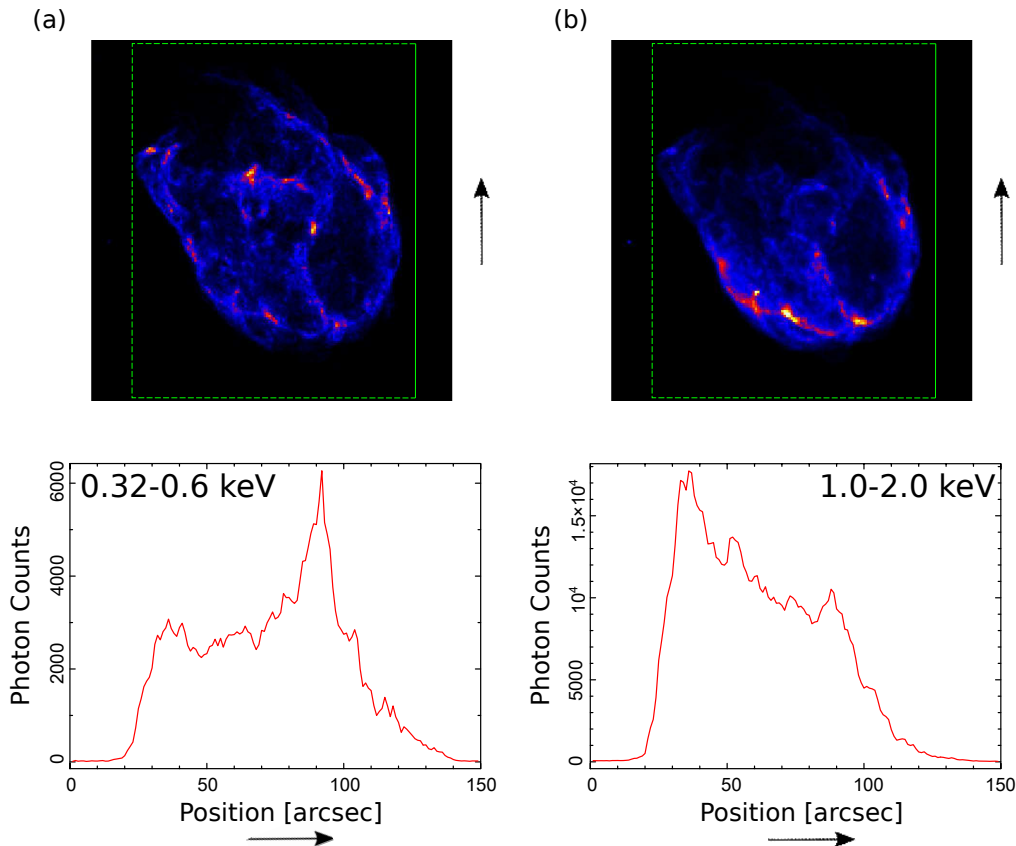


Figure 2. *Top:* Chandra ACIS flux images of N132D in the 0.32–0.6 keV band (a) and 1.0–2.0 keV band (b). The black arrows indicate the dispersion direction of the RGS for Obs. ID = 0157161001. The green rectangles are where the projection profiles given in the bottom panels are extracted. *Bottom:* Projected profiles of N132D in the energy bands corresponding to the top panel images. The profiles are largely different from each other.

with the ionization parameter and element abundances tied to those of the other components. We obtain a successful fit to these emission lines as well as the broadband spectra (Figure 3 red solid curve and Figure 4, respectively) with an improved C -stat/d.o.f. of 10426/7563. The best-fit parameters are given in Table 3. The constrained ionization parameter is significantly lower than $10^{12} \text{ cm}^{-2} \text{ s}$, indicating that the plasma is in the NEI. We also attempt to model the spectra with three-component CIE plasmas (`bvapec` model in XSPEC) and reach the results given in Table 4, confirming that the NEI (ionizing) plasma model indeed provides a better fit. No improvement is obtained when the initial plasma temperature kT_{init} of `bvrnei` is fixed to 3.0 keV assuming a recombining state.

Next we analyze the data from the other on-axis observations to investigate how the results depend on the Obs. ID with different spacecraft roll angles. Applying the same data reduction and spectral models, we obtain the electron temperatures and ionization timescale given in Figure 5 for each observation. Except for a few cases, the values are consistent within $\sim 10\%$ among the observations. We find that the Obs. ID 0157350201 data (roll angle = 196.82) give relatively high electron temperatures $kT_{e,\text{low}} \sim 0.27 \text{ keV}$, $kT_{e,\text{med}} \sim 0.67 \text{ keV}$. However, even if we fit the data with the fixed values of $kT_{e,\text{low}} = 0.2 \text{ keV}$ and $kT_{e,\text{med}} = 0.6 \text{ keV}$ (that are comparable to the values for the other Obs. IDs), the C -stat value only increases from 9582 to 9645 and the model still fits the data quite well. We therefore conclude that, regardless of the roll angle, the three-temperature model with kT_e of $\sim 0.2 \text{ keV}$, $\sim 0.6 \text{ keV}$, and $\sim 1.5 \text{ keV}$ gives a reasonable approximation of the observed spectrum that is extracted from the entire SNR. We also find that the elemental abundances have small variation among the Obs. IDs and their mean values (Figure 6) are comparable to the previous measurements of the LMC ISM (Hughes et al. 1998; Russell & Dopita 1992; Dopita et al. 2019). This suggests the swept-up ISM origin of the soft X-rays from this SNR, which is also supported by its shell-like morphology

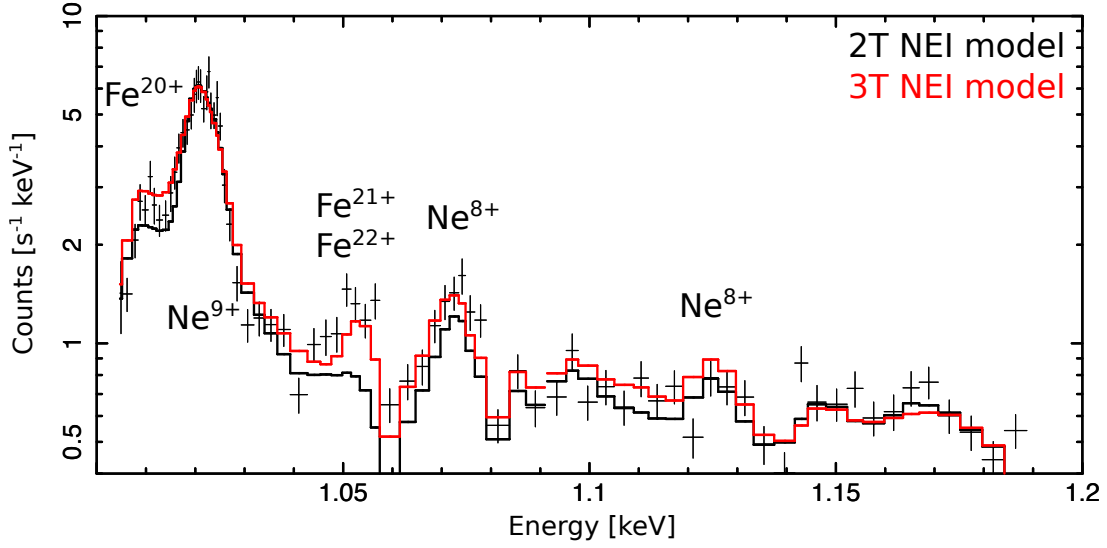


Figure 3. RGS1 second-order spectrum in the 1.0–1.2 keV band, fitted with the two-component (black) and three-component (red) NEI model. Only the latter successfully reproduces the emission lines of Fe^{21+} and Fe^{22+} around 1.05 keV.

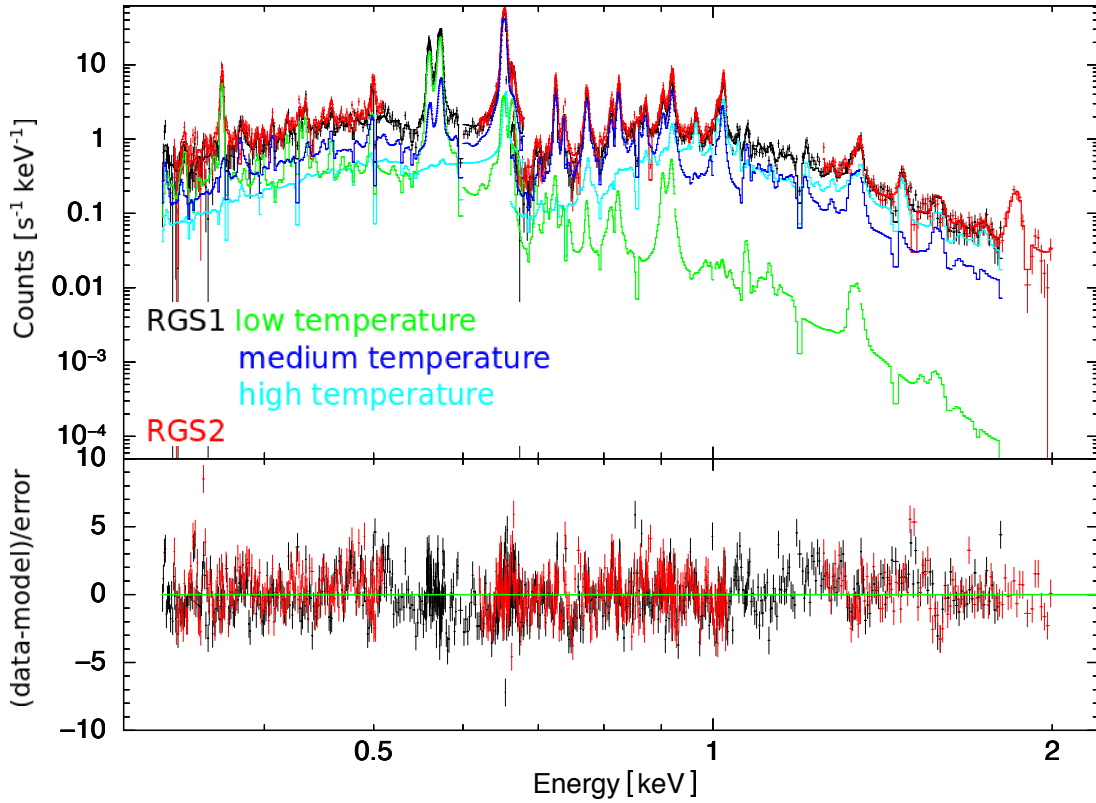


Figure 4. The RGS spectra fitted with the three-component NEI model. Black and red are the RGS1 and RGS2, respectively. The spectra below 0.68 keV are from the first-order data, whereas those above 0.66 keV are from the second-order data. The colored solid curves indicate the contribution of the individual components, low- T_e (green), medium- T_e (blue), and high- T_e (cyan) plasmas, to the RGS1 data. The bottom panel shows the residual from the best-fit model.

Table 3. The best-fit parameters of the three-temperature NEI model.

Parameters		
N_{H}	(10^{20} cm^{-2})	$6.8^{+0.1}_{-0.4}$
$kT_{e,\text{low}}$	(keV)	$0.200^{+0.004}_{-0.005}$
VEM_{low}	(10^{60} cm^{-3})	$1.31^{+0.03}_{-0.04}$
σ_{low}	(km s^{-1})	438 ± 34
v_{low}	(km s^{-1})	559 ± 18
$kT_{e,\text{med}}$	(keV)	$0.563^{+0.01}_{-0.005}$
VEM_{med}	(10^{60} cm^{-3})	$1.52^{+0.02}_{-0.03}$
σ_{med}	(km s^{-1})	445^{+21}_{-20}
v_{med}	(km s^{-1})	183 ± 11
$kT_{e,\text{high}}$	(keV)	$1.36^{+0.04}_{-0.02}$
VEM_{high}	(10^{60} cm^{-3})	$0.93^{+0.05}_{-0.03}$
σ_{high}	(km s^{-1})	0 (fixed)
v_{high}	(km s^{-1})	-639 ± 27
C		$0.26^{+0.02}_{-0.01}$
N		$0.172^{+0.009}_{-0.010}$
O		$0.34^{+0.01}_{-0.02}$
Ne		$0.51^{+0.02}_{-0.01}$
Mg		$0.49^{+0.03}_{-0.02}$
Si		0.59 ± 0.05
S		$0.57^{+0.06}_{-0.03}$
Ar		$0.75^{+0.09}_{-0.07}$
Ca		$0.04^{+0.12}_{-0.04}$
Fe		$0.411^{+0.014}_{-0.007}$
Ni		$0.71^{+0.11}_{-0.09}$
$n_e t$	($10^{10} \text{ cm}^{-3} \text{ s}$)	$9.8^{+0.3}_{-0.5}$
C -statistics/d.o.f.		10426/7563

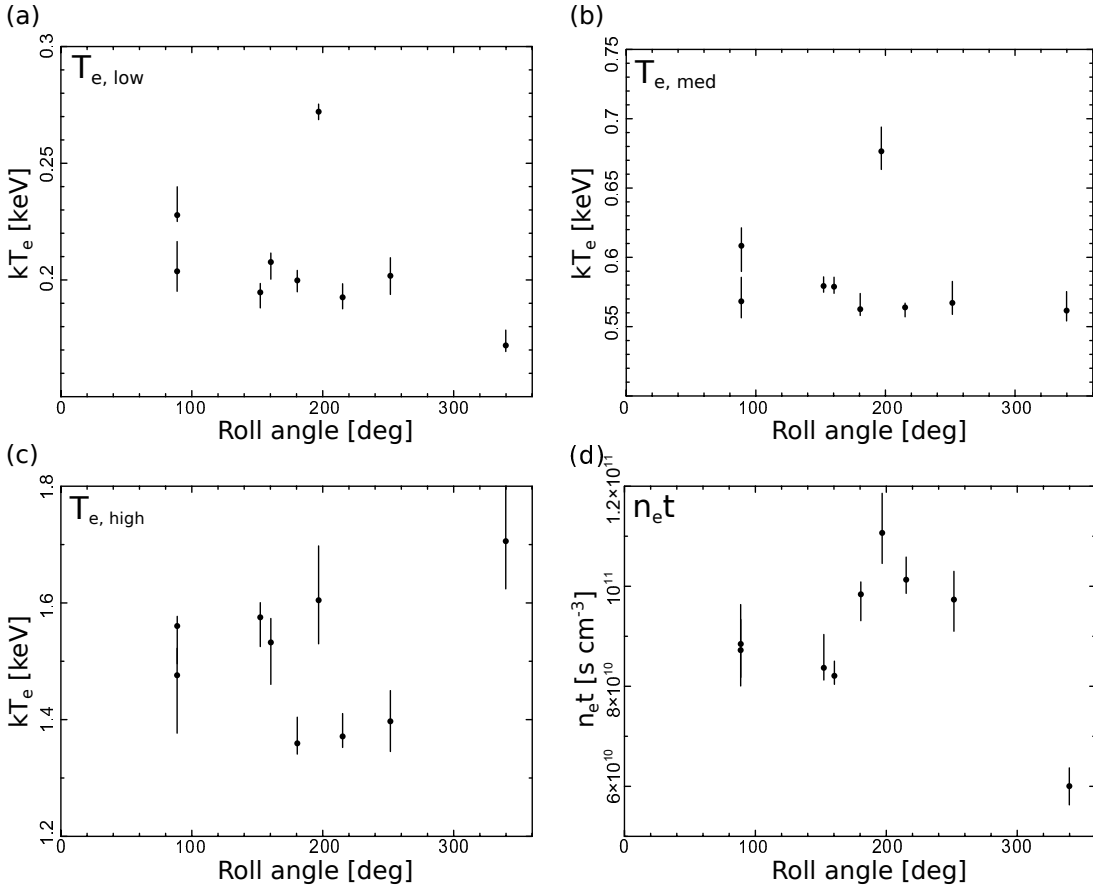
NOTE—The volume emission measure (VEM) is defined as $\int n_e n_H dV$, where n_e is the electron density, n_H the hydrogen density, and V the volume of the source. v is the line-of-sight bulk velocity of plasmas inferred from the Doppler shift of the emission lines. The velocity dispersion of the high temperature component (σ_{high}) is fixed because it is found to be consistent with 0.

at the energies below 2.0 keV (Figure 2). Strictly speaking, the Ca abundance is slightly lower than the typical value for the LMC. This may imply that a fraction of this element is depleted by dust grains, as is the case in e.g., Cas A (De Looze et al. 2017). An alternative possibility is that the L-shell line emissivity for Ca is inaccurate in the current atomic database.

Assuming a spherically symmetric shell with an outer radius of $R \sim 1'$ and a thickness of $R/12$ for the swept-up ISM, we obtain the plasma volume to be $8.7 \times 10^{58} \text{ cm}^3$ at the distance to the LMC. The VEM of each component derived from our spectral modeling (Table 3), therefore, corresponds to the post-shock proton density (n_{H}) and swept-up ISM mass (M_{ISM}) of 3.6 cm^{-3} and $260 M_{\odot}$ for the low- T_e component, 3.9 cm^{-3} and $280 M_{\odot}$ for the medium- T_e component, and 3.0 cm^{-3} and $220 M_{\odot}$ for the high- T_e component. These values are almost consistent with the previous

Table 4. Comparison of the best-fit parameters of the NEI and CIE cases.

	Ionizing	CIE
$kT_{e,low}$ (keV)	$0.200^{+0.004}_{-0.005}$	0.150 ± 0.003
$kT_{e,med}$ (keV)	$0.563^{+0.01}_{-0.005}$	0.379 ± 0.004
$kT_{e,high}$ (keV)	$1.36^{+0.04}_{-0.02}$	0.896 ± 0.007
kT_{init} (keV)	0.01 (fixed)	—
$n_e t$ ($\text{cm}^{-3} \text{s}$)	$(9.8^{+0.3}_{-0.5}) \times 10^{10}$	—
$C\text{-stat/d.o.f.}$	10426/7563	10570/7564

**Figure 5.** The best-fit electron temperatures and ionization timescale obtained from different observations.

measurements (e.g., [Hughes et al. 1998](#); [Williams et al. 2006](#)), although our estimate is based on some over-simplified assumptions (e.g., spherically symmetric shell, constant density over the whole SNR).

Figure 7 shows the line-of-sight velocity dispersion and bulk velocity for each Obs.ID, converted from the spectral line broadening and shift, respectively. The typical velocity dispersion is $400\text{--}500 \text{ km s}^{-1}$, consistent with the *Hitomi* measurement using the SXV emission ([Hitomi Collaboration et al. 2018a](#)). The redshift of the low- and medium-temperature components is comparable to the radial velocity of the LMC ISM at the region around this SNR ($275 \pm 4 \text{ km s}^{-1}$ [Vogt & Dopita 2011](#)). However, the dispersion among the observations is much larger than the typical

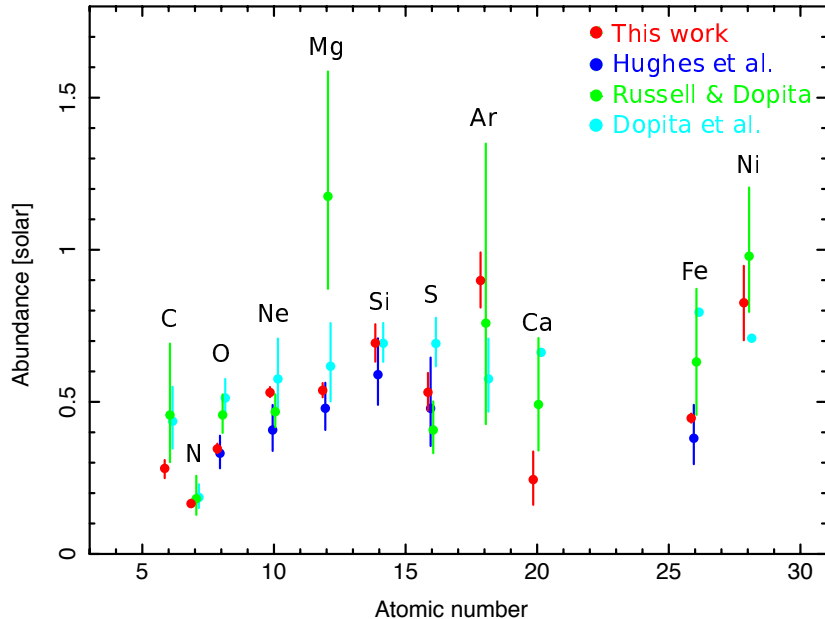


Figure 6. Elemental abundances (relative to the solar values of [Wilms et al. \(2000\)](#)) as a function of atomic number derived from our spectral analysis (red). The previous measurements by [Hughes et al. \(1998\)](#) (blue), [Russell & Dopita \(1992\)](#) (green), and [Dopita et al. \(2019\)](#) (cyan) are also normalized by the solar abundances of [Wilms et al. \(2000\)](#) and plotted for comparison.

statistical errors, implying that our measurements are dominated by the calibration uncertainties in the channel-to-wavelength transformation and/or incompleteness of our response generation for an extended source, rather than the real plasma motion. Although an accurate measurement of the line broadening and shift is crucial to understand the SNR kinematics, this is out of scope of the present work.

5. LINE DIAGNOSTICS AND DISCUSSION

In the previous subsection, our analysis has indicated that the plasma is in the NEI (ionizing) state ($n_e t \approx 10^{11} \text{ cm}^{-3} \text{ s}$), while [Behar et al. \(2001\)](#) did not distinguish between a CIE and NEI plasma. Here we reconfirm this result, based on more detailed spectral diagnostics that utilizes the well-resolved emission lines of O and Ne. The intensities of the resonance, forbidden, and $n = 3 \rightarrow 1$ transitions (hereafter “ r ”, “ f ”, and “ $\text{He}\beta$ ”, respectively) of O VII and Ne IX, and the O VIII and Ne X Ly α lines are directly measured with the following procedure⁵. First we modify one of the model data files that the XSPEC package includes, named `apex.v3.0.9_nei_line.fits`⁶, such that all the emission lines mentioned above are deleted (hereafter “modified NEI”). For each Obs.ID, the best-fit three-temperature NEI model obtained in Section 4 is replaced with a model consisting of the modified NEI plus eight Gaussians for the r , f , and $\text{He}\beta$ emission of O VII and Ne IX, and the Ly α emission of O VIII and Ne X. All the parameters (e.g., electron temperatures, elemental abundances) of the modified NEI components as well as the foreground absorption column are fixed to the best-fit values of the original three-temperature model. Then we fit the Gaussian components, obtaining the line fluxes for each Obs.ID in Table 5. Finally, we calculate the exposure-weighted mean flux (F) and their statistical errors ($\sigma_{F,\text{stat}}$), as well as the standard deviations among the different Obs.IDs ($\sigma_{F,\text{SD}}$)

⁵ A similar procedure was applied to the Fe K-shell emission from the Perseus Cluster by [Hitomi Collaboration et al. \(2018b\)](#) to estimate the effect of the resonance scattering in the cool core region of this object.

⁶ Usually found in the directory of `heasoft-6.24/spectral/modelData`.

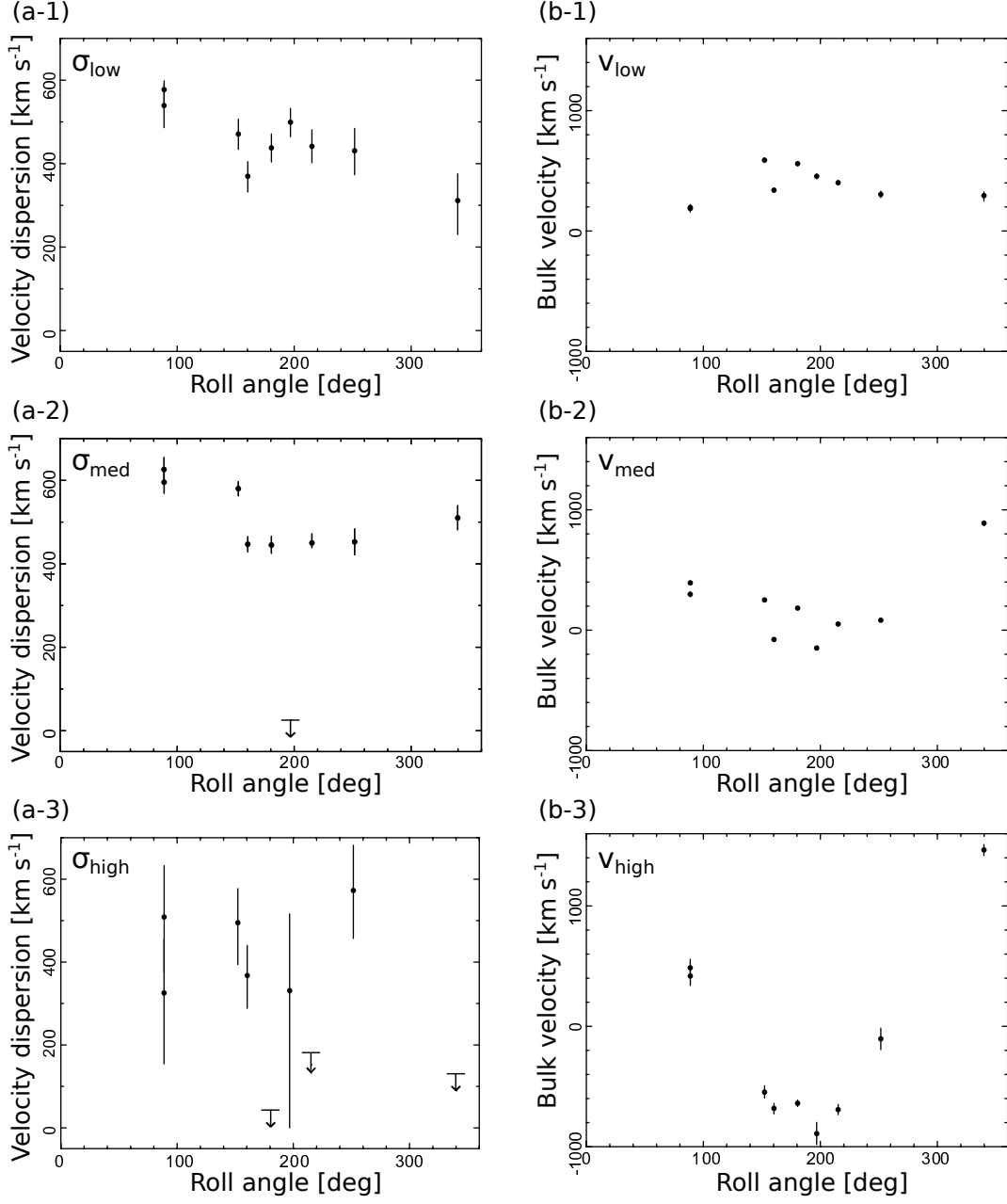


Figure 7. The line-of-sight velocity dispersion and bulk velocity for different observations. The values are subject to the uncertainties in the calibration of the relationship between the detector position and wavelength.

as follows:

$$\begin{aligned}
 F &= \frac{\sum_i F_i \times t_i}{\sum_i t_i} \\
 \sigma_{F,\text{stat}} &= \sqrt{\frac{(\sigma_i)^2 \times t_i}{\sum_i t_i}} \\
 \sigma_{F,\text{SD}} &= \sqrt{\frac{\sum_i (F_i - F_{\text{mean}})^2}{9}},
 \end{aligned} \tag{1}$$

Table 5. The intensities of the O and Ne emission.

Obs. ID	exposure time	O r	O f	O He β	O Ly α	Ne r	Ne f	Ne He β	Ne Ly α
	ksec	10^{-3}	10^{-3}	10^{-3}	10^{-2}	10^{-3}	10^{-3}	10^{-4}	10^{-3}
0125100201	13.63	6.99 ± 0.13	4.58 ± 0.18	1.31 ± 0.06	1.31 ± 0.01	2.73 ± 0.09	1.34 ± 0.08	5.46 ± 0.79	2.34 ± 0.08
0157160601	26.20	7.94 ± 0.19	5.30 ± 0.10	1.26 ± 0.03	1.36 ± 0.01	2.64 ± 0.07	1.40 ± 0.05	4.57 ± 0.54	2.37 ± 0.06
0157160801	29.09	9.17 ± 0.12	5.93 ± 0.13	1.29 ± 0.03	1.52 ± 0.01	2.79 ± 0.08	1.60 ± 0.05	4.55 ± 0.49	2.47 ± 0.06
0157161001	29.91	8.09 ± 0.10	5.61 ± 0.13	1.22 ± 0.04	1.40 ± 0.01	2.79 ± 0.06	1.33 ± 0.07	4.97 ± 0.42	2.39 ± 0.06
0157360201	15.02	8.48 ± 0.17	5.69 ± 0.17	1.38 ± 0.06	1.40 ± 0.02	2.43 ± 0.10	1.46 ± 0.08	5.98 ± 1.23	2.52 ± 0.08
0157360301	28.66	8.49 ± 0.12	5.79 ± 0.09	1.25 ± 0.03	1.49 ± 0.01	2.67 ± 0.07	1.59 ± 0.07	6.49 ± 0.56	2.44 ± 0.06
0157360501	14.92	7.99 ± 0.27	5.72 ± 0.16	1.31 ± 0.07	1.56 ± 0.01	2.78 ± 0.10	1.59 ± 0.10	4.10 ± 0.78	2.53 ± 0.08
0129341301	20.34	8.10 ± 0.15	5.57 ± 0.15	1.43 ± 0.04	1.41 ± 0.01	2.64 ± 0.07	1.48 ± 0.07	4.46 ± 0.61	2.43 ± 0.05
0137551101	15.04	8.55 ± 0.15	5.90 ± 0.13	1.37 ± 0.05	1.44 ± 0.02	2.63 ± 0.12	1.57 ± 0.07	5.44 ± 0.81	2.43 ± 0.07
Mean		8.27	5.60	1.30	1.44	2.69	1.48	5.11	2.43
Statistical error		0.17	0.16	0.05	0.01	0.08	0.07	0.67	0.07
Standard deviation		0.56	0.39	0.07	0.08	0.11	0.10	0.74	0.06

NOTE—In units of photons $\text{cm}^{-2}\text{s}^{-1}$

Table 6. The mean line intensity ratios.

	He β / He α	Ly α / He α	f/r
O	0.094 ± 0.004	1.04 ± 0.02	0.68 ± 0.02
Ne	0.12 ± 0.02	0.58 ± 0.02	0.55 ± 0.03

where F_i , σ_i , and t_i are the line flux, its statistical error, and exposure of the observation i . The resulting values are given in Table 5.

The line ratios given in Table 6 offer useful diagnostics for the plasma condition. The He β /He α ratio (where He α is defined to be the sum of the resonance and forbidden lines) almost solely depends on the electron temperature, whereas the Ly α /He α ratio reflects the charge balance between the H-like and He-like ions (so-called “ionization temperature”). The forbidden-to-resonance ratio depends not only on both electron and ionization temperatures but also on external effects, such as resonance scattering (e.g., Miyata et al. 2008) and charge exchange (e.g., Uchida et al. 2019). The black curves in Figure 8 (a-1) and (b-1) are the theoretically predicted He β /He α ratios of O and Ne (for CIE plasmas), as a function of the electron temperature, derived using PyAtomDB⁷. The observed line ratios (green areas) are compared with these theoretical values, constraining the characteristic electron temperatures to 0.28–0.33 keV for O and >0.68 keV for Ne. We also estimate the electron temperatures based on the He β / r or He β / f ratio, instead of He β /He α , and find that the constrained values do not change significantly. Similarly, the observed Ly α /He α ratios (that represent the ionization temperature) are compared with the theoretical ratios for CIE plasmas in Figure 8 (a-2; for O) and (b-2; for Ne). The obtained ionization temperature (~ 0.24 keV for O; ~ 0.39 keV for Ne) is lower than the characteristic electron temperature of each element, confirming that the plasma is in the ionizing state.

The black curve in Figure 8 (a-3) shows the O VII f/r ratio as a function of the electron temperature that is expected for a CIE plasma. We find that the observed f/r ratio (green area) corresponds to 0.23–0.26 keV, significantly lower than the characteristic electron temperatures determined by the He β /He α ratio (panel a-1). The gap between the two temperatures becomes even larger, when the observed f/r ratio is compared with the theoretical values for an

⁷ <https://github.com/AtomDB/pyatomdb>

ionizing plasma with $n_e t = 10^{11} \text{ cm}^{-3} \text{ s}$ (red curve; the best-fit ionization parameter for the three-component NEI model). Similar results are obtained for the Ne IX f/r ratio (Figure 8 b-3). These discrepancies could be just due to the complexity of the multiple-temperature plasmas, whose spectrum cannot be perfectly reproduced by our approximated three-temperature model. We find, however, that the discrepancies remain even if the ionization timescale and elemental abundances (in addition to the electron temperature) are untied among the three components (Figure 9). It would, therefore, be worth discussing another possibility that the observed f/r ratios are modified by other effects, such as resonance scattering and charge exchange.

5.1. Resonance Scattering

The effect of resonance scattering is usually negligible in SNRs, since their plasmas are optically thin. However, if the column density of certain ions is relatively high, some of the resonance line photons can be scattered out from the line of sight when propagating in the X-ray emitting plasma itself (e.g., Miyata et al. 2008; Amano et al. 2020). Since N132D exhibits a dense SNR shell in the soft X-ray band (Behar et al. 2001; Borkowski et al. 2007) and its geometry is known to depart from spherical symmetry (e.g., Law et al. 2020), it is indeed possible that resonance scattering has taken place and modified the observed f/r ratio. Based on this assumption, we revisit the full-band RGS spectra and conduct the following analysis. In addition to the best-fit three-temperature model obtained in Section 4, we include two Gaussians at 0.574 keV and 0.922 keV (corresponding to the O VII and Ne IX resonance lines, respectively) in the spectral fitting by allowing their normalization to have negative values. This analysis yields the C -stat value of 10412 (reduced from 10426) and Gaussian normalizations (the mean of the nine Obs.IDs) of $-4.7 (\pm 1.5) \times 10^{-4}$ photons $\text{cm}^{-2} \text{ s}^{-1}$ for O VII r and $-1.6 (\pm 0.8) \times 10^{-4}$ photons $\text{cm}^{-2} \text{ s}^{-1}$ for Ne IX r . Both are indeed smaller than zero, as implied by Figure 8 a-3 and b-3. If the optical depth (τ) for the line photons is significantly smaller than unity, the relationship between the scattered and observed photon flux (ΔI and I_{obs} , respectively) is given as $\Delta I \approx \tau I_{\text{obs}}$. Thus, attributing the negative Gaussian normalizations to the resonance scattering, we obtain $\tau_{\text{O},r} = 0.057 \pm 0.018$ and $\tau_{\text{Ne},r} = 0.059 \pm 0.030$.

Theoretically, the cross section of the resonance scattering is given as $\sigma \sim 1.3 \times 10^{-9} \cdot f/E \cdot (m_i/kT_i)^{1/2} \text{ cm}^2$, where f , E , m_i , and T_i are the oscillator strength of the line transition, photon energy in keV, and the mass and temperature of the ions, respectively (e.g., Miyata et al. 2008). The optical depth for the resonance scattering can, therefore, be expressed as

$$\begin{aligned} \tau &= \sigma n_z L \\ &= 1.3 \times 10^{-9} \cdot \frac{f}{E} \left(\frac{m_i}{kT_i} \right)^{1/2} A_Z \left(\frac{n_z}{n_Z} \right) \left(\frac{n_Z}{n_{\text{H}}} \right)_{\odot} n_{\text{H}} L, \end{aligned} \quad (2)$$

where n_z is the ion density (that is assumed to be constant along the line of sight), L is the physical depth of the plasma, A_Z is the abundance of the element Z relative to the solar value of Wilms et al. (2000), n_Z is the element density, and n_{H} the hydrogen density; thus n_z/n_Z and $(n_Z/n_{\text{H}})_{\odot}$ represent the ion fraction of the ion z and the solar abundance of the element Z , respectively. Table 7 gives the coefficients we are now interested in. We refer to the AtomDB database (available via PyAtomDB) to obtain the oscillator strengths and ion fractions. For the latter, the ionization temperatures constrained in Figure 8 (a-2) and (b-2) are applied. Since the resonance line of O VII is dominated by the low- T_e component (see Figure 4), we apply the hydrogen density of 3.6 cm^{-3} , obtained in the previous section. Similarly, we assume $n_{\text{H}} = 3.9 \text{ cm}^{-3}$ for the Ne IX resonance line that is dominated by the medium- T_e component. Using the mean elemental abundances obtained in Figure 6, and assuming $kT_i = kT_e$ for both components, we obtain the plasma depth L of $1.4 \times 10^{18} \text{ cm}$ and $5.9 \times 10^{18} \text{ cm}$ for the low- T_e (O VII) and medium- T_e (Ne IX) components, respectively. Therefore, if the resonance scattering is fully responsible for the anomaly in the f/r ratio, the depth of the medium- T_e component must be about four times larger than that of the low- T_e component. Both depth are $\lesssim 15\%$ of the SNR radius, reasonable for the region where the resonance scattering takes place.

5.2. Charge Exchange

Given the presence of the dense molecular clouds at the periphery of N132D (e.g., Williams et al. 2006; Sano et al. 2015; Dopita et al. 2018), charge exchange between highly-charged ions and neutral atoms or molecules would be a possible alternative that is responsible for the enhanced f/r ratio. In fact, evidence for charge exchange has been observed in several other SNRs that are interacting with dense clouds (e.g., Pup A, Cygnus Loop: Katsuda et al.

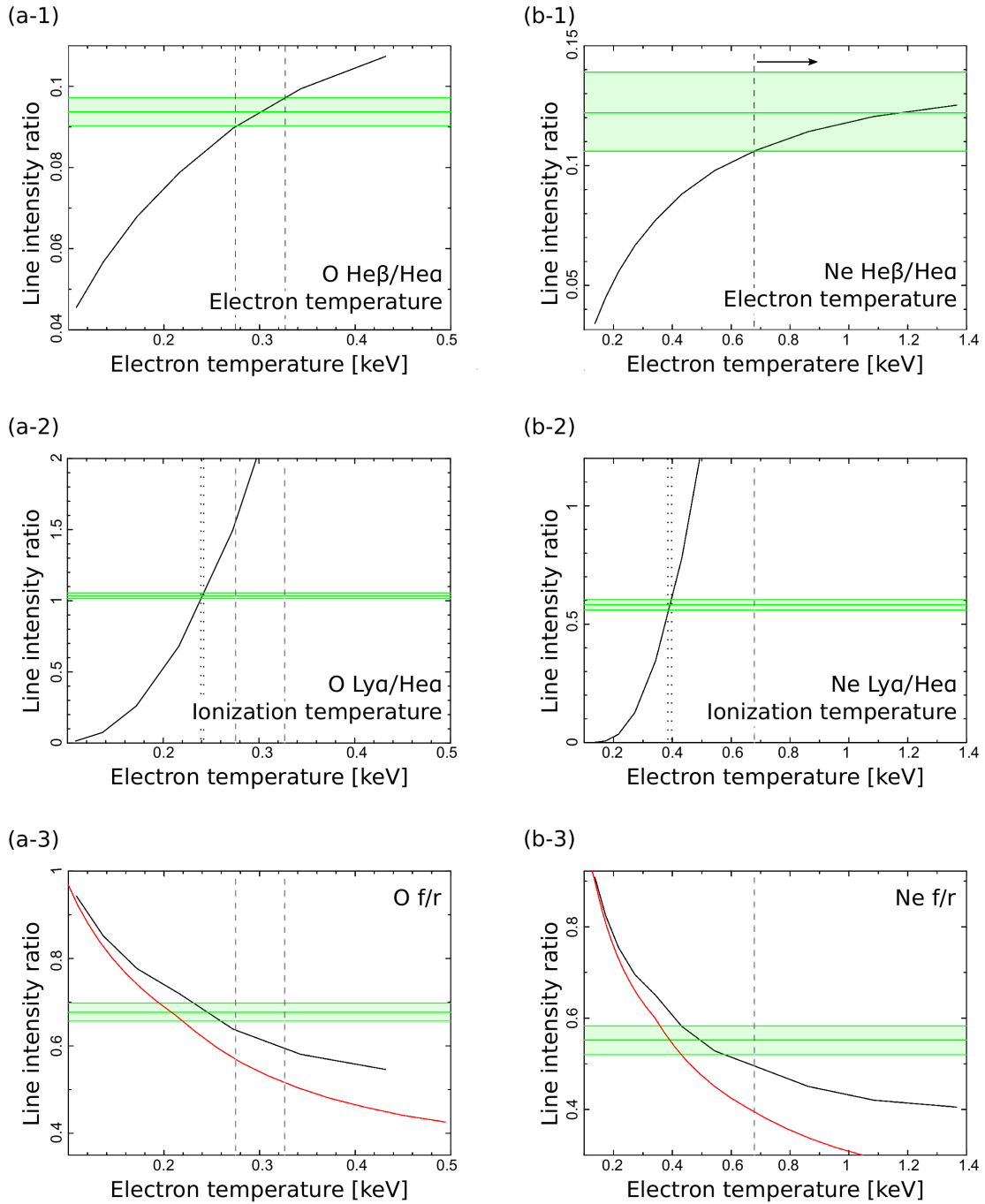


Figure 8. Comparison between the theoretical and observational ratios of the diagnostic emission lines. (a-1): O He β /He α ratio that represents the electron temperature, where He α is defined as the sum of O VII resonance and forbidden lines. (a-2): O Ly α /He α ratio that represents the ionization temperature. (a-3): O forbidden-to-resonance line ratio. Panels (b-1), (b-2), and (b-3) are the same as (a-1), (a-2), and (a-3), but for Ne. The black curves are the theoretically-predicted ratios as a function of the electron temperature, derived using PyAtomDB assuming CIE. The red curves in panels (a-3) and (b-3) are those expected for NEI plasmas with $n_e t = 10^{11} \text{ cm}^{-3} \text{ s}$. The green areas indicate the observed line ratios. The dashed and dotted lines indicate the constrained electron and ionization temperatures, respectively.

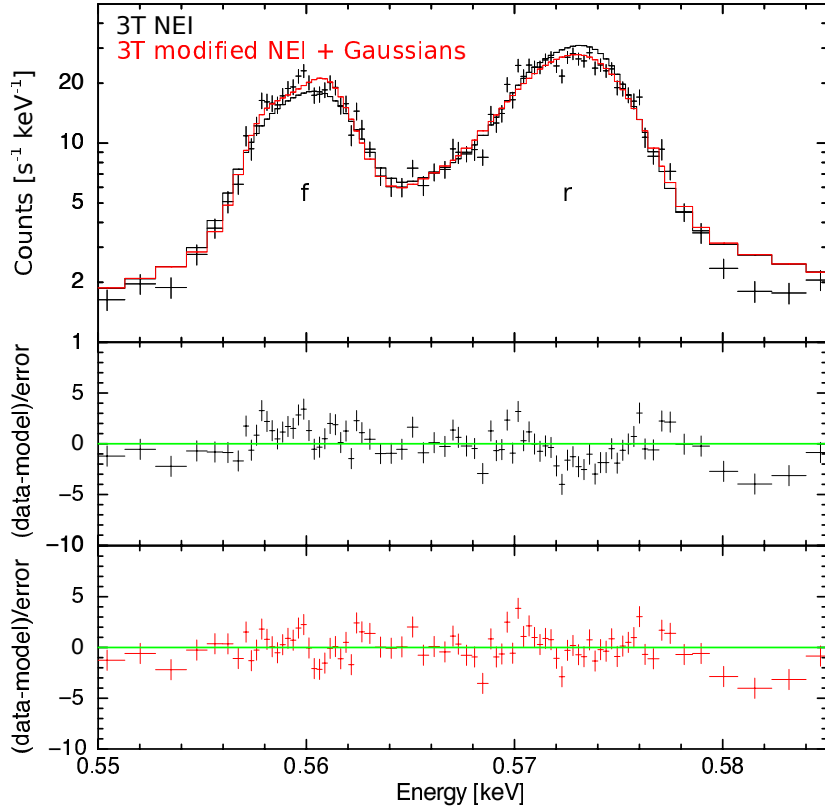


Figure 9. The RGS1 spectrum of the O VII He α emission. The black curve in the top panel is the best-fit three-temperature NEI model, where not only the electron temperature but also the ionization timescale and O abundance of each component are independently fitted. The red curve is the model consisting of modified NEI and Gaussians (see text). The middle and bottom panels show the residual between the model and data corresponding to the black and red curves in the top panel, respectively.

Table 7. Coefficients for the resonance scattering estimate.

	f	n_z/n_Z	$(n_z/n_H)_\odot$	A_Z	n_H
O VII r	0.720	0.13	4.90×10^{-4}	0.35	3.6
Ne IX r	0.742	0.29	8.71×10^{-5}	0.53	3.9

NOTE— f is the oscillator strength. A_Z is the abundance relative to the solar value. The unit of the last column is cm^{-3} .

2012; Uchida et al. 2019). We thus fit the full-band spectra from the deepest observation (Obs.ID: 0157161001) with the AtomDB-based charge exchange model (`vacx`: Smith et al. 2012), in addition to the three-component NEI model. Specifically, we introduce a `vacx` model by assuming the ionization temperatures of O and Ne to be 0.24 keV and 0.39 keV, respectively (based on Figure 8 a-2 and b-2). The O and Ne in this component are treated as free parameters. The parameter ‘`model`’ that determines the (n, l) distribution of the exchanged ions⁸ is set to the default value ‘8’, but this does not affect the results significantly. The addition of the charge exchange components slightly

⁸ n and l are the principal quantum number and orbital angular momentum, respectively. See http://www.atomdb.org/CX/acx_manual.pdf for more details.

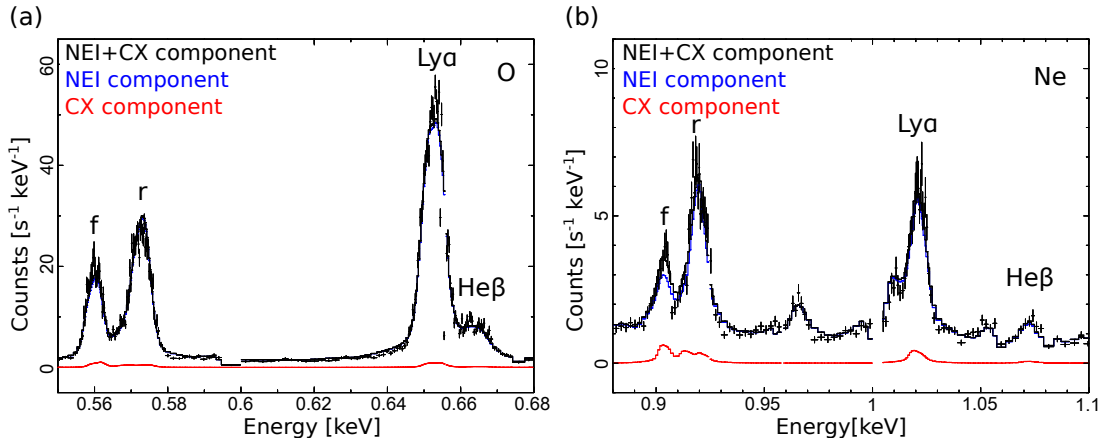


Figure 10. RGS1 spectrum around the O emission (a) and Ne emission (b), fitted with the model consisting of the three-temperature NEI (blue) and charge exchange (red) components.

improves the C-stat value from 10426 to 10417 (when all the parameters of the NEI components are fixed to the original best-fit values) or 10393 (when the parameters given in Table 3 are allowed to vary). The close-up spectra around the O and Ne emission are shown in Figure 10, where the contribution of the charge exchange components is indicated by the red curves. The deficit in the forbidden line flux in the NEI component is partially compensated by the charge exchange component.

The volume emission measure of the charge exchange component, defined as $\int n_{\text{H}} n_{\text{H}^0} dV$, is obtained to be $1.4 \times 10^{33} \text{ cm}^{-3}$, where n_{H} is the density of hydrogen in the hot plasma, n_{H^0} the density of neutral hydrogen, and V the volume where the charge exchange takes place. Assuming $n_{\text{H}} = 3.6\text{--}3.9 \text{ cm}^{-3}$ (obtained in the previous section) and $n_{\text{H}^0} = 100 \text{ cm}^{-3}$ (Dopita et al. 2018), we estimate the volume of the charge exchange interaction region to be $3.6\text{--}3.8 \times 10^{30} \text{ cm}^3$. Although charge exchange is expected to occur only in a narrow layer immediately behind the shock front (up to a few percents of the SNR radius: e.g., Lallement 2004), the obtained volume is too small compared with the volume of the swept-up ISM ($\sim 8.7 \times 10^{58} \text{ cm}^3$). Therefore, if the f/r ratio is enhanced solely by charge exchange, it is required for this process to take place only in local small regions, such as the south rim where the SNR forward shock is interacting with the molecular clouds (Sano et al. 2015). The abundances of O and Ne are obtained to be $0.14^{+0.58}_{-0.10}$ and $1.4^{+0.06}_{-0.49}$, respectively. The latter is about three times higher than the Ne abundances of our best-fit NEI components as well as the LMC average. This result, together with the small volume of the charge exchange interaction region, may suggest that the charge exchange scenario is less likely as the origin of the enhanced f/r ratio, although the uncertainties in the currently available charge exchange models are relatively large.

5.3. Caveats and Future Prospects

We have demonstrated that the high-resolution RGS spectra of N132D can reasonably be reproduced by the three-temperature plasmas in the NEI state plus the contributions of resonance scattering and/or emission induced by charge exchange (although the latter scenario requires an extremely small volume of the interaction region). However, it is not yet conclusive whether these effects are indeed at work, since our three-temperature model is only an approximation of the more realistic multiple-temperature plasma. The observations that enable spatially-resolved spectral analysis are crucial to provide conclusive evidence of these effects. If the resonance scattering indeed contributes to the observed spectrum, the resonance line flux is expected to be reduced most significantly at the region with the highest plasma column density. If the charge exchange is dominant, on the other hand, a spatial correlation between the forbidden-line enhancement and the ambient density is expected. We actually search for such evidence by extracting monochromatic images of O VII r and f emission from the first-order RGS data as was done by Uchida et al. (2019), but no significant spatial variation in the f/r ratio is found, owing to the insufficient spatial resolution and statistics. It should also be noted that the physics of charge exchange is still highly uncertain in both theoretical and observational aspects. Future improvement in the charge exchange models will help provide better constraints on the physics of SNR-ISM interaction with high-resolution spectroscopy.

6. CONCLUSIONS

We have presented high-resolution spectroscopy of N132D, the X-ray brightest SNR in the LMC, utilizing the XMM–Newton RGS data accumulated to date. The L-shell emission lines of Ar, Ca, and other elements have been detected from this SNR, for the first time. To enable quantitative analysis, we have generated spectral responses as carefully as possible, by taking into account the roll angle and wavelength dependences on the line spread function. The 0.3–2.0-keV spectrum can be well reproduced by the three-temperature optically-thin thermal plasmas in the NEI (ionizing) state, which reasonably approximates more realistic multiple-temperature plasmas. The measured elemental abundances are comparable to the average values of the LMC ISM, confirming that the soft X-rays from this SNR are dominated by the swept-up ambient medium. The second-order RGS spectra, which we have analyzed for the first time, have successfully resolved the forbidden and resonance lines of Ne IX, allowing us to perform detailed plasma diagnostics using these lines. The observed forbidden-to-resonance flux ratios of O VII and Ne IX are slightly higher than expected for the typical NEI plasma. Either resonance scattering and/or charge exchange emission may account for this enhancement, although spatially-resolved high-resolution spectroscopy with future missions, like the *Athena* X-ray Integral Field Unit (X-IFU: Barret et al. 2018), is necessary to provide conclusive evidence.

ACKNOWLEDGMENTS

We thank Yoshitomo Maeda, Shinya Yamada, and Hikaru Suzuki for their helpful advice on data analysis and discussion. This work is partially supported by Grants-in-Aid for Scientific Research (KAKENHI) of the Japanese Society for the Promotion of Science (JSPS) grant Nos., 19H00704 (HY) and 19K03915 (HU).

REFERENCES

- Acero, F., Ackermann, M., Ajello, M., et al. 2016, *ApJS*, 224, 8
- Ackermann, M., Albert, A., Atwood, W. B., et al. 2016, *A&A*, 586, A71
- Amano, Y., Uchida, H., Tanaka, T., Gu, L., & Tsuru, T. G. 2020, arXiv e-prints, arXiv:2005.04626
- Bamba, A., Ohira, Y., Yamazaki, R., et al. 2018, *ApJ*, 854, 71
- Barret, D., Lam Trong, T., den Herder, J.-W., et al. 2018, in *Society of Photo-Optical Instrumentation Engineers (SPIE) Conference Series*, Vol. 10699, Proc. SPIE, 106991G
- Behar, E., Rasmussen, A. P., Griffiths, R. G., et al. 2001, *A&A*, 365, L242
- Blair, W. P., Morse, J. A., Raymond, J. C., et al. 2000, *ApJ*, 537, 667
- Borkowski, K. J., Hendrick, S. P., & Reynolds, S. P. 2007, *ApJL*, 671, L45
- Cash, W. 1979, *ApJ*, 228, 939
- Chen, Y., Zhang, F., Williams, R. M., & Wang, Q. D. 2003, *ApJ*, 595, 227
- De Looze, I., Barlow, M. J., Swinyard, B. M., et al. 2017, *MNRAS*, 465, 3309
- den Herder, J. W., Brinkman, A. C., Kahn, S. M., et al. 2001, *A&A*, 365, L7
- Dickey, J. M., & Lockman, F. J. 1990, *ARA&A*, 28, 215
- Dopita, M. A., Seitzzahl, I. R., Sutherland, R. S., et al. 2019, *AJ*, 157, 50
- Dopita, M. A., Vogt, F. P. A., Sutherland, R. S., et al. 2018, *ApJS*, 237, 10
- Favata, F., Vink, J., Parmar, A. N., Kaastra, J. S., & Mineo, T. 1997, *A&A*, 324, L45
- H. E. S. S. Collaboration, Abramowski, A., Aharonian, F., et al. 2015, *Science*, 347, 406
- Hitomi Collaboration, Aharonian, F., Akamatsu, H., et al. 2018a, *PASJ*, 70, 16
- . 2018b, *PASJ*, 70, 10
- Hughes, J. P., Hayashi, I., & Koyama, K. 1998, *ApJ*, 505, 732
- Katsuda, S., Tsunemi, H., Mori, K., et al. 2012, *ApJ*, 756, 49
- Lallement, R. 2004, *A&A*, 422, 391
- Law, C. J., Milisavljevic, D., Patnaude, D. J., et al. 2020, arXiv e-prints, arXiv:2004.00016
- Mathewson, D. S., Ford, V. L., Dopita, M. A., et al. 1983, *ApJS*, 51, 345
- Miceli, M., Orlando, S., Burrows, D. N., et al. 2019, *Nature Astronomy*, 3, 236
- Miyata, E., Masai, K., & Hughes, J. P. 2008, *PASJ*, 60, 521
- Morse, J. A., Winkler, P. F., & Kirshner, R. P. 1995, *AJ*, 109, 2104
- Pietrzyński, G., Graczyk, D., Gieren, W., et al. 2013, *Nature*, 495, 76

- Rasmussen, A. P., Behar, E., Kahn, S. M., den Herder, J. W., & van der Heyden, K. 2001, *A&A*, 365, L231
- Russell, S. C., & Dopita, M. A. 1992, *ApJ*, 384, 508
- Sano, H., Fukui, Y., Yoshiike, S., et al. 2015, *Astronomical Society of the Pacific Conference Series*, Vol. 499, *Revealing the Large-Scale Structures of Interstellar Gas Associated with the Magellanic SNR N132D*, ed. D. Iono, K. Tatematsu, A. Wootten, & L. Testi, 257
- Schenck, A., Park, S., & Post, S. 2016, *AJ*, 151, 161
- Sharda, P., Gaetz, T. J., Kashyap, V. L., & Plucinsky, P. P. 2020, *ApJ*, 894, 145
- Smith, R. K., Foster, A. R., & Brickhouse, N. S. 2012, *Astronomische Nachrichten*, 333, 301
- Uchida, H., Katsuda, S., Tsunemi, H., et al. 2019, *ApJ*, 871, 234
- Vink, J., Laming, J. M., Gu, M. F., Rasmussen, A., & Kaastra, J. S. 2003, *ApJL*, 587, L31
- Vogt, F., & Dopita, M. A. 2011, *Ap&SS*, 331, 521
- Williams, B. J., Borkowski, K. J., Reynolds, S. P., et al. 2006, *ApJL*, 652, L33
- Wilms, J., Allen, A., & McCray, R. 2000, *ApJ*, 542, 914
- Yamaguchi, H., Eriksen, K. A., Badenes, C., et al. 2014, *ApJ*, 780, 136